Detection efficiency of microchannel plates for e⁻ and π⁻ in the momentum range from 17.5 to 345 MeV/c

M. Tulej, S. Meyer, M. Lüthi, D. Lasi, A. Galli, L. Desorgher, W. Hajdas, S. Karlsson, L. Kalla, and P. Wurz

View Online   **Export Citation**   **CrossMark**

Detection efficiency of microchannel plates for e⁻ and π⁻ in the momentum range from 17.5 to 345 MeV/c

M. Tulej,[1,a] S. Meyer,[1] M. Lüthi,[1] D. Lasi,[1] A. Galli,[1] L. Desorgher,[2] W. Hajdas,[2] S. Karlsson,[3] L. Kalla,[3] and P. Wurz[1]

[1]*Space Research and Planetary Sciences, Physics Institute, University of Bern, CH-3012 Bern, Switzerland*
[2]*Laboratory of Particle Physics, Paul Scherrer Institute, CH-5232 Villigen, Switzerland*
[3]*Swedish Institute of Space Physics, Space Kampus 1, Kiruna, Sweden*

High-energy e⁻ and π⁻ were measured by the multichannel plate (MCP) detector at the PiM1 beam line of the High Intensity Proton Accelerator Facilities located at the Paul Scherrer Institute, Villigen, Switzerland. The measurements provide the absolute detection efficiencies for these particles: 5.8% ± 0.5% for electrons in the beam momenta range 17.5–300 MeV/c and 6.0% ± 1.3% for pions in the beam momenta range 172–345 MeV/c. The pulse height distribution determined from the measurements is close to an exponential function with negative exponent, indicating that the particles penetrated the MCP material before producing the signal somewhere inside the channel. Low charge extraction and nominal gains of the MCP detector observed in this study are consistent with the proposed mechanism of the signal formation by penetrating radiation. A very similar MCP ion detector will be used in the Neutral Ion Mass (NIM) spectrometer designed for the JUICE mission of European Space Agency (ESA) to the Jupiter system, to perform measurements of the chemical composition of the Galilean moon exospheres. The detection efficiency for penetrating radiation determined in the present studies is important for the optimisation of the radiation shielding of the NIM detector against the high-rate and high-energy electrons trapped in Jupiter's magnetic field. Furthermore, the current studies indicate that MCP detectors can be useful to measure high-energy particle beams at high temporal resolution. © *2015 AIP Publishing LLC.* [http://dx.doi.org/10.1063/1.4928063]

I. INTRODUCTION

The Particle Environment Package (PEP) is an instrument suite of the scientific payload of European Space Agency's (ESA) JUICE mission to the Jupiter system.[1] PEP will conduct remote global imaging of the Jupiter environment with *in situ* measurements of electrons, ions, and energetic neutrals in the particle energy range spanning over nine decades (0.001 eV to 1 MeV). The results of the investigation will help understand the interaction of the Jupiter magnetosphere with Galilean moons.

The neutral ion mass (NIM) instrument is a time-of-flight (TOF) mass spectrometer, which is one of the instruments of PEP, designed to measure charged and neutral atoms and molecules present in the exospheres of Jovian moons. NIM will record mass spectra within the mass range 1–1000 amu with a mass resolution (m/Δm) close to 1100. The laboratory tests show that by acquiring spectra for 5 s at 10^{-10} mbar vacuum conditions, a detection threshold of $\sim 10^{-16}$ mbar can be reached.[2–4] To achieve the required sensitivity, NIM uses highly sensitive multichannel plate (MCP) ion detector. Nevertheless, the presence of a substantial fraction of particles (electrons and protons) trapped by Jupiter's magnetic fields (radiation belts) with the energy distribution exceeding hundreds of MeV imposes high radiation tolerance requirements on the instruments and can deteriorate their

performance and lifetime because of radiation-induced effects.[5–10] Understanding the interaction effects of this radiation with various materials is essential to optimally design NIM and its shielding against penetrating radiation and to interpret the measured mass spectra. Although modelling techniques are continuously improving, not all the input parameters they require are easily accessible, in particular, the behaviour of detectors subjected to high-rate high-energy particle beams. Therefore, we performed the current radiation tests. They allowed us to characterise the sensitivity of the MCP detector to high energy radiation and to identify the different signatures of particle species.

MCP detectors are compact electron multipliers supporting high gain and measurements with high spatial and temporal resolution.[11,12] In the majority of applications, they are used to measure charged and neutral particles including electrons, protons, molecular ions, and photons in the optical, X-ray energy range, and gamma-ray energy range.[13–15] They are used also to measure neutrons, positrons, and pions.[16–18] The mechanism underlying signal generation in MCPs was investigated in several theoretical studies.[13,19–29] The detection efficiency of MCPs to various particles is a function of mass, charge, and particle energy and to perform quantitative measurements, the relevant calibration studies are required.[15,30]

So far, the detection efficiency to electrons was investigated in the energy range 0.05–100 keV.[19,31–34] For the incident electrons with the energies within a few keV, the detection efficiency can rise up to 75%. The open area is found to contribute mostly to the detected signals.[19] The detection

a)Author to whom correspondence should be addressed. Electronic mail: marek.tulej@space.unibe.ch

efficiency to electrons (or positrons) in the range 60–100 keV is observed to decline to about 16% which is interpreted as a decrease of the secondary electron emission coefficient of the active MCP materials.[18,35]

In the current contribution, the MCP detection efficiencies to e^-, μ^-, and π^- in the beam momentum range 17.5–345 MeV/c are investigated. The applied electron fluxes and energies are close to those expected in the Jupiter environment. Hence, the results obtained in these investigations form the basis for detailed testing of the performance of the MCP detector in similar conditions as those in the Jovian environment.

II. EXPERIMENTAL SETUP

A. PSI proton beam facility and peripheral instrumentation

The studies were conducted at the High Intensity Proton Accelerator Facility, PSI Villigen, Switzerland using the secondary beam line, PiM1.[36] The PiM1 beamline is designed to deliver charged pions ($\pi^\pm$), electrons and positrons ($e^\pm$), muons ($\mu^\pm$), and protons (p) to the experimental area. These particles are produced by the interaction between a small fraction of the 590 MeV high intensity proton beam and a thin graphite target. Polarity and momentum of secondary particles are controlled by the currents in the magnet of the beam delivery system and can be changed by command. The entrance of the PiM1 beam line is oriented at an angle of 22° to the proton primary beam line. The quadrupole and dipole magnets of the PiM1 beam line are used to select and transport the particles to the experimental area, where they are focused by the last magnetic quadrupoles at the location of the MCP detector. The distance of the whole beam line from the M-target to the focus point is 23.65 m. There are no electrostatic separators and the PiM1 beam always contains a mixture of e, μ, and π particles. For the current experiment, only the negative polarity of the beam was selected.

The PiM1 beam is typically used for high-energy π and μ experiments in the beam momenta range 100–300 MeV/c. The present investigation is one among the first, where the electron fraction of the beam was of primary interest. Therefore, additional beam diagnostic measurements were necessary to characterise the beam geometry, composition, and flux at the momenta range relevant to the current application. A part of the results from the diagnostic studies relevant to the present measurements is presented in Sec. III A and more details can be found in our recent report.[36]

The measurements by the MCP detector were conducted with instrumentation located in two rooms: the measurement room and the control room. Fig. 1 displays schematically the locations of peripheral instrumentation and principles of the method of synchronisation applied in this study. The MCP detector and the signal acquisition oscilloscope 2 were placed in the measurement area whereas the high-voltage power supply and oscilloscope 1 collecting a pulse train from the ionisation chamber representative for the beam current were located in the control room. The signals generated by the MCP detector were collected by a digital storage oscilloscope
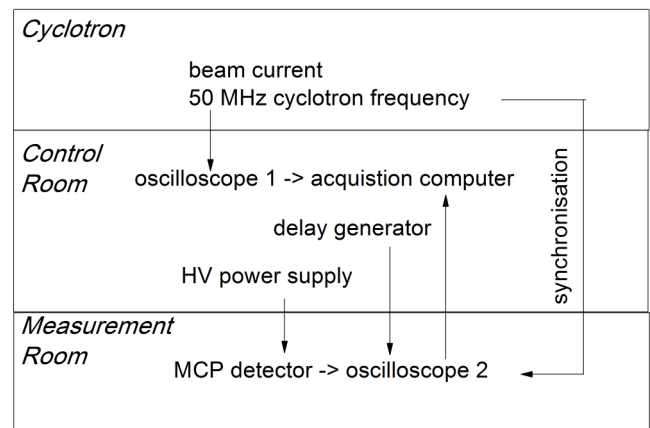

FIG. 1. Schematic of the experimental arrangement and applied synchronisation between the cyclotron frequency and the measurements by the MCP detector.

(oscilloscope 2) within a recording time window controlled by a delay generator (SRS DG535). The measurements were synchronised with the 50 MHz cyclotron operation frequency. Oscilloscope 2 acquired 100 ns long waveforms at a rate of 10 GS/s but the signals produced by the MCP detector were measured within the first 20 ns of the acquisition window.

Measurements of individual MCP waveforms were triggered when a pulse signal with an amplitude larger than $\Delta V_{MCP} = -2.5$ mV was produced by the MCP detector. The trigger level was chosen by considering the results from the analysis of the pulse height distribution (PHD) of a background radiation measurement. For the background radiation measurement, a negative exponential was obtained with a mean value of pulse amplitude of -2.2 mV (nominal gain: 4.8×10^5). The trigger level has been set to the slightly lower value of -2.5 mV and almost all pulses could be measured within the available oscilloscope measurement window. The duration of the measurements was constrained by available beam time therefore the time of individual measurement was optimised to obtain the counting rate statistics with the error smaller than 5%. In addition, the individual measurements were repeated three times to control the reproducibility of the counting statistics.

Fig. 2 displays the part of the measurement room where the particle measurements were conducted. At location (A),
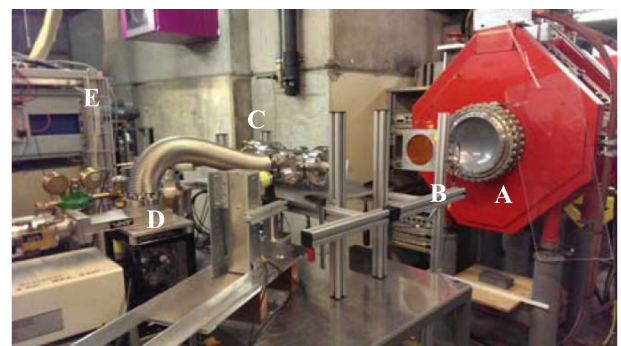

FIG. 2. Experimental area: (A) particle beam exit location, (B) ionisation chamber for beam current monitoring, (C) vacuum chamber with a MCP detector, (D) pumping system, and (E) electronic racks: signal acquisition oscilloscope and communication ports.
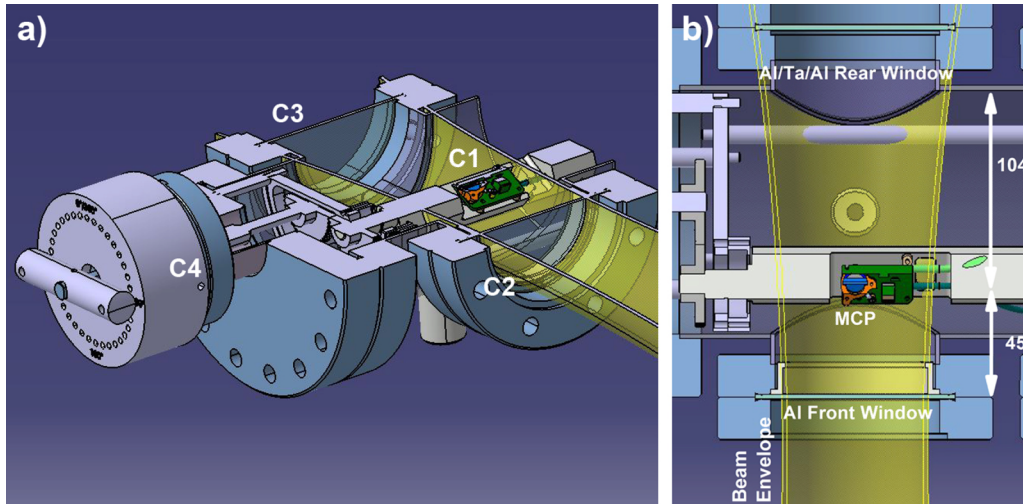
FIG. 3. (a) Left panel: cut through the design drawing of the experimental vacuum chamber with a schematic envelope of the particle beam penetrating the vacuum chamber (yellow tubular feature): the MCP detector (C1), entrance window (C2), rear window (C3), and the rotating assembly (C4); (b) right panel: positioning of MCP in the vacuum chamber with the predicted shape of the penetrating particle beam.

the particle beam leaves the beam guiding system and is focused ~1 m away from the exit plane, at the measurement location (C). The ionisation chamber (B) is placed approximately 800 mm away from the beam exit location and sufficiently close to the MCP detector location that the full beam passes through the area of this detector. The ionisation chamber monitors the variation of the primary beam current in real time, and the results are synchronised with the proton current pulse used to produce secondary particles (e, μ, and π) at carbon foil target. The experimental vacuum chamber (C) with the MCP detector inside is located approximately ~200 mm from the ionisation chamber.

The MCP detector is kept in a cylindrical vacuum chamber which is pumped down to pressures below 10^{-6} mbar by turbomolecular and rotary pumps (D). The detector is mounted on a rotating rod to vary the angle of incidence relative to the incident particle beam (Fig. 3, left panel). In all the present measurements, however, the front MCP plate was mounted always perpendicularly to the incident particle beam. The circular entrance window has a diameter of 50 mm and is made from 2 mm thick aluminium foil. The beam diameter depends on the beam momentum (see also Table II). At the focal plane, the beam size is comparable to or smaller than the window diameter. Hence, it is expected that the full beam passed through the window. The MCP detector is located 45 mm behind the front window and 104 mm from the rear window (see also Fig. 3, right panel). The latter is made from a composite stack of Al (2 mm), Ta (10 mm), and Al (1 mm) plates. The rear window shielding was prepared for set of measurements which are not discussed here.

B. MCP detector characteristics

The detector is custom-made for the NIM instrument of PEP for the JUICE mission and consists of two MCPs purchased from Photonis® USA that are mounted in a chevron configuration. The outside diameter of a single rimless MCP is 10.16 ± 0.08 mm with the quality diameter 8.00 mm. The thickness of single MCP is 0.61 ± 0.03 mm and the material

type is specified as Long-Life™ MCP-10 armed in Nichrome (80/20) electrode material with the electrode penetration within 0.3-0.7 channel diameter. The center-to-center spacing is 12 μm, the pore size is 10 μm, and the bias angle is $8° \pm 1°$. MCPs are combined with a home-made anode which is coupled to a 50 Ω transmission line. The MCP detector allows for signal amplification in the range 10^6 to 10^7 for nominal ion detection. The MCP stack resistance is close to 470 MΩ as is measured in our laboratory. The typical value for the open area ratio is stated to be larger than 55% by Photonis. The open area ratio for the MCPs used in the present experiment is close to 67%. Nevertheless, the area ratio parameter is not considered in our analysis. Fig. 4 displays the electronic schematic of the MCP electronic circuit used in the present investigation.

The anode is a gold plated printed circuit board (PCB) structure with a diameter of 10 mm impedance-matched to 50 Ω and to a 10 nF DC-block capacitor. The other side of this capacitor is directly welded and straight-line connected to a high-frequency sub-miniature-A (SMA) vacuum feedthrough.
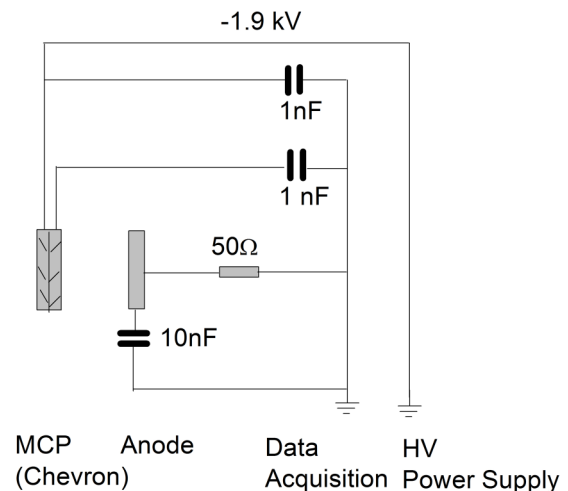

FIG. 4. Schematic of the electronic circuit used in the MCP detector.

The signal line is shielded to match 50 Ω impedance and to minimize noise pickup. The standard potential of −1.9 kV is applied to the front MCP. A 180 V zener-diode is used in series to control the potential difference between the back MCP and the anode.[37] Two 1 nF capacitors deliver the charge to MCPs.[38] The typical single ion event produces a pulse width (FWHM) of approximately 900 ps for this custom-made detector. The MCP detector circuit applied here only measures negatively charged particles, e.g., secondary electrons, when their energies exceed 1.9 keV because the entrance window is biased negatively.

C. Measurement methodology

To obtain the absolute detection efficiency of the MCP detector (η_{MCP}), we have to determine the incident particle rate ($k_{Incident}$) at the front MCP and the MCP detection counting rates (k_{MCP}). The absolute MCP detection efficiency is defined as

$$\eta_{MCP}(E_i) = 100 * \frac{k_{MCP}(E_i)}{k_{Incident}(E_i)} \, [\%].$$

The incident particle rate $k_{Incident}$ [#counts/s] for each investigated particle beam is derived from the results of the beam diagnostic measurements.[36] The MCP detector was placed subsequently at a close location to measure the PHD for each of investigated particles and to determine the MCP particle rates from the PHD analysis. To account for losses of the primary beam and the effects due to interaction of primary incident beam with experimental chamber (secondary particle production), the modelling studies were performed. The modelling results provide means for the corrections to the incident and measured MCP counting rates.

III. RESULTS AND DISCUSSION

A. Primary particle beam

1. Beam characteristics

Several instruments available at the PiM1 facility were used to monitor beam characteristics including ionisation chamber, NaI(Tl) scintillator detector, E − ΔE plastic scintillator telescope, and the beam scanner. The ionisation chamber measured total intensity of the beam and monitored a variation of the beam intensity during the experiment. NaI(Tl) was used with a front anti-coincidence thin plastic detector to determine gamma-ray background and the E − ΔE plastic scintillator telescope was used to monitor electrons.

The e⁻, µ⁻, and π⁻ particles are produced at a carbon target for each primary proton pulse and the beam guiding system selected particles of the same momentum. The particles of different masses separate readily into well-isolated bunches while travelling from the production target to the experiment location and TOF method was applied to determine the beam composition (Table I). For the range of beam momenta applied in this study, the electrons have relativistic velocities and arrive first at the detectors while the arrival times for µ⁻ and π⁻ are the function of the applied beam momentum. The measurements show that for beam momenta lower than 115 MeV/c, the beam is composed mainly of e⁻ (Table I) whereas for the momenta larger than 115 MeV, the fraction of π⁻ particles increases and for the beam momenta larger than 200 MeV/c, the π⁻ particle fraction becomes the dominant contribution. The µ⁻ fraction could be quantified only for momenta up to 200 MeV/c. More details on the applied methods are described in our recent report.[36]

The beam geometry (including beam centre and planar particle distribution intensity at the beam focal plane) as well as beam flux and intensity were measured using a beam scanner system, consisting of a plastic scintillator detector mounted on a XY-translation stage. A Gaussian particle distribution in X and Y direction was measured and the beam cross section area was found to be slightly elliptical (Table II). The beam flux and intensity are directly related to the incident proton beam current. Table II and Fig. 5 summarise the parameters of the particle beam determined from the measurements for various beam momenta. Note that the beam geometry depends on the beam momentum and the beam waist (σ_x, σ_y) at the focal point (FWHM) decreases with an increase of the beam momenta (tighter focussing). Also, the central position (x_0, y_0) of the beam (maximum of the beam intensity) moves slightly for different beam momenta.

TABLE I. Beam momentum, kinetic energy, and beam fractions of the e⁻, µ⁻, and π⁻ determined from the TOF measurements.[36] Here, m_0 is the rest mass.

Beam momentum (MeV/c)	Kinetic energy (MeV)			Fraction (%)		
	e⁻ $m_0 c^2 = 0.512$ MeV	µ⁻ $m_0 c^2 = 105.658$ MeV	π⁻ $m_0 c^2 = 139.57$ MeV	e⁻	µ⁻	π⁻
17.25	16.746	1.399	1.062	100	0	0
23	22.494	2.474	1.882	100	0	0
28.75	28.243	3.842	2.930	100	0	0
57.5	56.990	14.633	11.380	100	0	0
86.25	85.740	30.734	24.500	100	0	0
115	114.489	50.511	41.275	97.46	0.67	1.87
143.75	143.26	72.748	60.789	83.77	2.07	14.16
172.5	171.989	96.629	82.322	63.16	2.37	34.47
201.25	200.79	121.646	105.341	46.44	2.15	51.41
230	229.489	147.450	129.465	30.44	0	69.56
287.5	286.988	200.642	180.017	13.96	0	86.04
345	344.488	255.159	232.592	6.9	0	93.1

TABLE II. Characteristics of PiM1 beam at the focal plane position. Typical beam current value is close to 2.1 mA.[36] Here, (x_0, y_0) define the beam central position and beam waist is described by (σ_x, σ_y).

Beam momentum (MeV/c)	Maximal flux/beam current (no. of particles/s cm^{-2} mA^{-1}) $\times 10^3$	Intensity/beam current (no. of particles/s mA^{-1}) $\times 10^6$	x_0 (cm)	y_0 (cm)	σ_x (cm)	σ_y (cm)
17.25	0.721	0.116	−0.55	−1.73	4.44	5.6
23	2.57	0.328	−0.92	−1.47	3.85	5.47
34.5	15.6	1.16	−0.73	−0.54	2.82	4.1
57.5	78.8	3.080	−0.47	−0.24	2.21	2.82
86.25	169	5.130	−0.48	−0.51	1.79	2.19
115	242	5.180	−0.38	−0.74	1.88	1.84
230	687	9.670	−0.37	−1.04	1.81	1.26
345	1090	12.200	−0.59	−1.1	1.74	1.07

2. Incident particle rate at the MCP surface

The incident particle rate at the MCP surface (MCP Ø = 8 mm, open area ratio 67%) is derived from the beam diagnostic data presented in Tables I and II. For the calculation, the maximal beam flux and the beam current averaged over the MCP measurement duration and normalized to the standard beam current were applied. The typical ideal primary particle rates at the front MCP are shown in Fig. 6. The transmission losses and secondary particles including gamma rays, electrons, and positrons were not considered. The electron rate is found to be significant in the entire momentum range 50–345 MeV/c and is on the order of 10^5 counts/s. The μ^- particles were detected in the beam momenta range 100–200 MeV/c with the rate close to 10^4 counts/s. The rate of π^- particles is observed to increase with the beam momentum and becomes larger than 10^5 counts/s for beam momenta above 175 MeV/c.

To account for changes of the primary particle rates at the MCP entrance surface due to the interaction with the materials of the experimental setup, modelling calculations were conducted using GRAS/Geant4 modelling tools.[39,40] In these simulations a full 3D geometry setup was used that includes air gap after beam monitor, vacuum chamber, and manipulator mechanism (Fig. 7). No detailed detector assembly was implemented; instead, a vacuum target sphere was included in the location of the MCP detector. The primary beams for the simulations were constructed using data given in Tables I and II. For some beam momenta, the beam parameters were derived by linear interpolation. All data in this section are normalised to 2.1 mA beam current.

The calculations provide the total particle flux and the fraction of different species at target sphere as the function of the primary beam momentum (Table III). The effects of the interaction of primary electrons with the materials of the experimental setup are more significant than those due
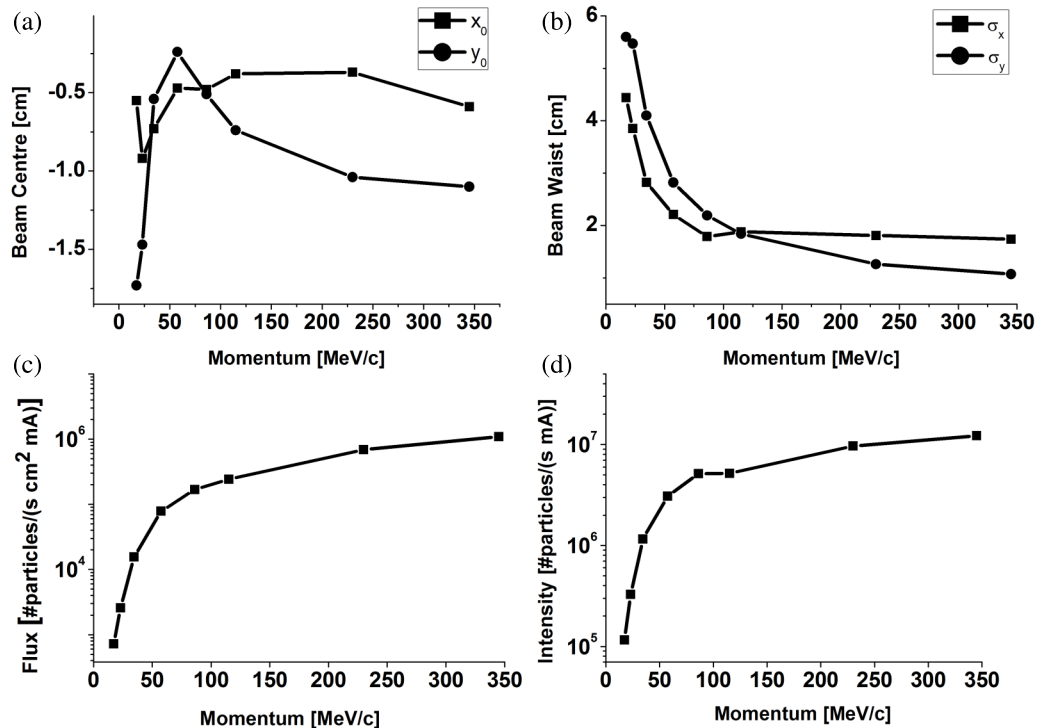

FIG. 5. Characteristics of PiM1 beam at exit focus position as determined by PSI instruments:[36] (a) beam central position, (b) beam waist, (c) flux at the centre of the beam, and (d) total beam intensity.
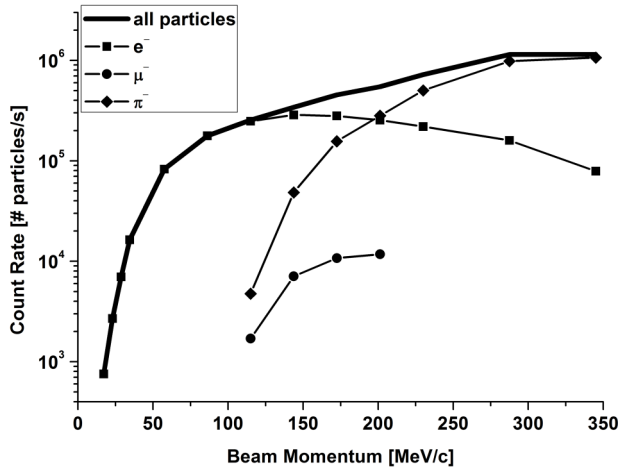
FIG. 6. Calculated primary particle rates at the MCP entrance surface taking into account the flux values determined from the diagnostic measurements without the corrections due to transmission losses and presence of secondary particles.

FIG. 7. Visualisation from Geant4/GRAS simulation with primary beam e⁻ 11.5 MeV/c (e⁻ tracks are shown in red and gamma tracks in cyan colours, respectively).

to primary muons and pions. The μ^- and π^- particles are expected to lose energy mainly by excitation and ionisation and the transmission losses for these particles are low in the investigated beam momenta range. In contrast, the electron transmission losses are larger and the primary beam generate substantial fraction of secondary particles (e^+, e^-, γ) (see Tables III–V). The rate of secondary electrons is observed to rise systematically in the investigated beam momenta range. The modelling results indicate that primary electrons are a main source of secondary electrons for the beam momenta lower than 150 MeV/c (see Fig. 6). For larger beam momenta the primary electron rate decreases and the rate of pions becomes larger than the electron rate. Pions start to contribute to the secondary electron rate for the beam momenta larger than ~90 MeV/c. For the beam momentum close to 345 MeV/c, this contribution is about 73% and the rest of secondary electrons are produced by the primary electrons. Fig. 8 displays the flux dependence on the calculated energy distribution of the secondary electrons in the function the primary electron momentum. A sharp peak (maximum of the electron flux) of
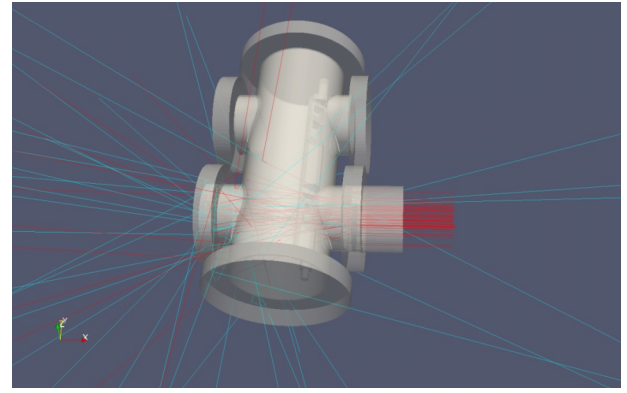
the flux distribution is observed at primary electron energies. While for primary electron momenta smaller than 40 MeV/c, a slow decrease of the secondary electron flux with the secondary electron energy decrease is observed down to the energies 20–30 keV; for the primary electron momenta larger than 40 MeV/c, it is calculated to be relatively constant with the secondary electron energy decrease in this range. For the secondary electron energies smaller than 20 keV, the flux decreases readily with the decrease of their energies for all investigated energies of the primary electron momenta.

The primary electrons lose also energy via production of gamma rays (Bremsstrahlung). For electron energies larger than critical energy (for aluminium, the critical energy is 47 MeV), the second mechanism of energy loss is opened by electron-positron pairs production.[41] The rate of gamma rays is readily correlated with the primary electron rate (Table III). The calculations predict also a small flux of e^+ due to (e^-–e^+) pair production via interaction of gamma rays with surrounding materials (Table III). The energy distribution of gamma rays at the target sphere obtained from the calculations shows a clear cutoff near the primary electron energy (Fig. 9).

TABLE III. GRAS/Geant4 registered particles fluxes and fractions of different species at the MCP location from the incident primary particles.

Beam momentum (MeV/c)	Total flux at MCP location (no. of particles/s cm^{-2}) × 10^3	Fraction of total flux at MCP location				
		e^+ (%)	e^- (%)	γ (%)	μ^- (%)	π^- (%)
11.5	1.56	0.0	70.0	30.0	0.0	0.0
17.25	2.88	0.1	64.5	35.4	0.0	0.0
23	10.1	0.1	61.2	38.6	0.0	0.0
28.75	63.7	0.2	60.9	38.8	0.0	0.0
57.5	288	0.4	64.3	35.3	0.0	0.0
86.25	676	0.4	69.1	30.6	0.0	0.0
115	755	0.4	68.1	29.9	0.4	1.2
143.75	964	0.3	61.7	26.9	1.5	9.5
172.5	1420	0.2	50.8	21.9	2.0	25.1
230	1640	0.1	28.5	14.3	0.4	56.7
287.5	1950	0.1	15.3	9.5	0.4	74.7
345	2290	0.1	9.2	6.8	0.4	83.6

TABLE IV. GRAS/Geant4 calculated total flux of secondary products and fraction of different species at MCP location that are produced by the interaction of primary particles with surrounding materials.

Beam momentum (MeV/c)	Flux of secondary products (particle/s cm^{-2}) $\times 10^3$	Fraction of secondary products at MCP location				
		e$^+$ (%)	e$^-$ (%)	γ (%)	μ$^-$ (%)	π$^-$ (%)
11.5	0.545	0.1	14.3	85.6	0.0	0.0
17.25	1.17	0.1	12.5	87.3	0.0	0.0
23	4.42	0.3	11.5	88.2	0.0	0.0
28.75	28	0.5	11.3	88.2	0.0	0.0
57.5	117	0.9	12.3	86.7	0.0	0.0
86.25	240	1.0	13.0	86.0	0.0	0.0
115	262	1.1	12.7	86.2	0.0	0.0
143.75	303	1.0	13.0	85.6	0.3	0.1
172.5	370	0.9	14.0	83.9	0.8	0.3
230	301	0.7	17.5	78.0	2.1	1.6
287.5	261	0.6	22.6	71.0	3.1	2.6
345	240	0.5	28.1	64.8	3.8	2.8

The majority of the secondary products that reach the target sphere are originating from the incoming electrons that interact with the aluminium front window. There is also a part that is produced in material behind the MCP which is probably mostly from the rear window that include a tantalum plate. The contribution of these secondary products is essential at lower beam momenta but when the momentum is higher these becomes less important (see Table V).

Estimation of the rate at the front MCP that has active surface perpendicular to the beam is done by assuming the majority of the particles from this simulation are incident on the MCP surface at right angles, either from rear or front. Fig. 10 displays the expected particle fluxes at the MCP detector.

B. MCP measurements

1. TOF analysis by MCP detector

After characterising the particle beam, the MCP detector was placed in the measurement chamber to study the MCP signals induced by the high-energy particles. Fig. 11 summarises the measurements; panel (a) displays the typical waveforms containing the event pulses measured by the MCP detector and displayed by the oscilloscope 2 and panel (b) displays the cyclotron waveforms recorded simultaneously with the MCP measurement. The measurements of the e$^-$, μ$^-$, or π$^-$ particles were synchronised with the 50 MHz cyclotron frequency. Based on the phase shift between the measured MCP pulses and the cyclotron waveform, three groups of pulses and some few uncorrelated measurement events were obtained. The latter are background events from cosmic rays or natural decay of radioactive elements in MCP, random high energy particles from the facility, and background particles induced by the incident particle beam. Because of the relativistic speeds of the primary electrons, their pulses were measured at a nearly constant phase shift relative to the sinusoidal cyclotron waveform for all of the beam momenta. In contrast, the μ$^-$ and π$^-$ particles are much heavier thus slower and arrive at the MCP detector at different times. For small values of beam momenta, the flight times of the μ$^-$ and π$^-$ particles are longer, and these particles can be detected only within the following cyclotron period of T = 20 ns, and their phase shifts have to be corrected accordingly.

TABLE V. Particle rate at MCP positioned with active surface perpendicular to the beam direction.

| Beam momentum (MeV/c)	Rate at MCP location (particles/s) 0.5026 cm^2 cross section (Ø 8 mm MCP)					
	e$^+$	e$^-$	Gamma	μ$^-$	π$^-$	Total
11.5	1.44×10^{-01}	$5.48 \times 10^{+02}$	$2.35 \times 10^{+02}$	$0.00 \times 10^{+00}$	$0.00 \times 10^{+00}$	$7.83 \times 10^{+02}$
17.25	8.78×10^{-01}	$9.36 \times 10^{+02}$	$5.13 \times 10^{+02}$	$0.00 \times 10^{+00}$	$0.00 \times 10^{+00}$	$1.45 \times 10^{+03}$
23	$5.99 \times 10^{+00}$	$3.10 \times 10^{+03}$	$1.96 \times 10^{+03}$	$0.00 \times 10^{+00}$	$0.00 \times 10^{+00}$	$5.07 \times 10^{+03}$
28.75	$7.22 \times 10^{+01}$	$1.95 \times 10^{+04}$	$1.24 \times 10^{+04}$	$0.00 \times 10^{+00}$	$0.00 \times 10^{+00}$	$3.20 \times 10^{+04}$
57.5	$5.42 \times 10^{+02}$	$9.33 \times 10^{+04}$	$5.12 \times 10^{+04}$	$0.00 \times 10^{+00}$	$0.00 \times 10^{+00}$	$1.45 \times 10^{+05}$
86.25	$1.26 \times 10^{+03}$	$2.35 \times 10^{+05}$	$1.04 \times 10^{+05}$	$0.00 \times 10^{+00}$	$0.00 \times 10^{+00}$	$3.40 \times 10^{+05}$
115	$1.45 \times 10^{+03}$	$2.58 \times 10^{+05}$	$1.14 \times 10^{+05}$	$1.69 \times 10^{+03}$	$4.50 \times 10^{+03}$	$3.79 \times 10^{+05}$
143.75	$1.50 \times 10^{+03}$	$2.99 \times 10^{+05}$	$1.31 \times 10^{+05}$	$7.32 \times 10^{+03}$	$4.62 \times 10^{+04}$	$4.85 \times 10^{+05}$
172.5	$1.67 \times 10^{+03}$	$3.63 \times 10^{+05}$	$1.56 \times 10^{+05}$	$1.40 \times 10^{+04}$	$1.80 \times 10^{+05}$	$7.14 \times 10^{+05}$
230	$1.09 \times 10^{+03}$	$2.35 \times 10^{+05}$	$1.18 \times 10^{+05}$	$3.13 \times 10^{+03}$	$4.68 \times 10^{+05}$	$8.26 \times 10^{+05}$
287.5	$8.31 \times 10^{+02}$	$1.51 \times 10^{+05}$	$9.30 \times 10^{+04}$	$4.08 \times 10^{+03}$	$7.34 \times 10^{+05}$	$9.82 \times 10^{+05}$
345	$6.60 \times 10^{+02}$	$1.06 \times 10^{+05}$	$7.80 \times 10^{+04}$	$4.52 \times 10^{+03}$	$9.60 \times 10^{+05}$	$1.15 \times 10^{+06}$
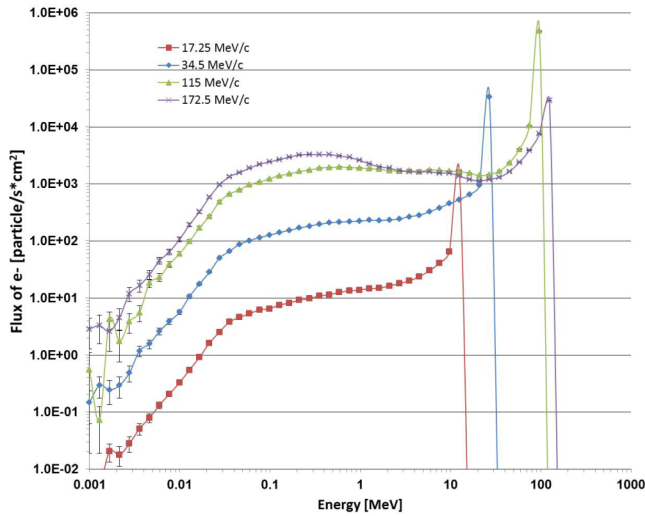
FIG. 8. Electron energy distribution at the MCP location for selected beam momenta of the primary electron beam.

FIG. 10. Particle rate at MCP positioned with active surface perpendicular to the beam direction.

The assignment of the group pulses is made by using TOF principle. Knowing the particle's mass, momentum, and distance from the production target to the MCP detector location ($\Delta s = 23.65$ m), the flight times of a particular particle can be derived and correlated with the phase shift of the measured pulse groups. In Fig. 11, panel (c) displays the results from the measurements of the e^-, μ^-, or π^- particles for the beam momentum 149.5 MeV/c and the phase shifts obtained from the TOF calculation are indicated by vertical lines. The events that could not be attributed to any of these three groups of pulses are denoted as "background pulses" and can originate from the interaction of the MCP detector with high-energy environmental radiation of the facility, cosmic rays, or even from trace radioactive elements.[42] The events due to the secondary radiation produced by the interaction of the primary particles with the surrounding materials are measured by the MCP detector within times similar to that of the primary incident particles because of the close proximity of the surrounding material. Hence, the secondary electrons
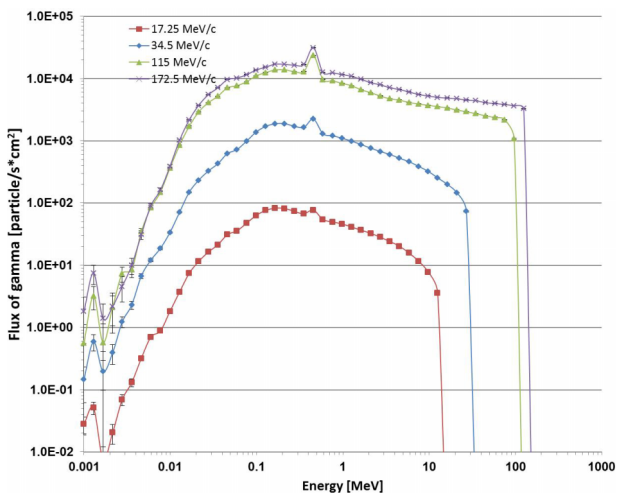

FIG. 9. Energy distribution of secondary gammas at the MCP location for selected beam momenta.
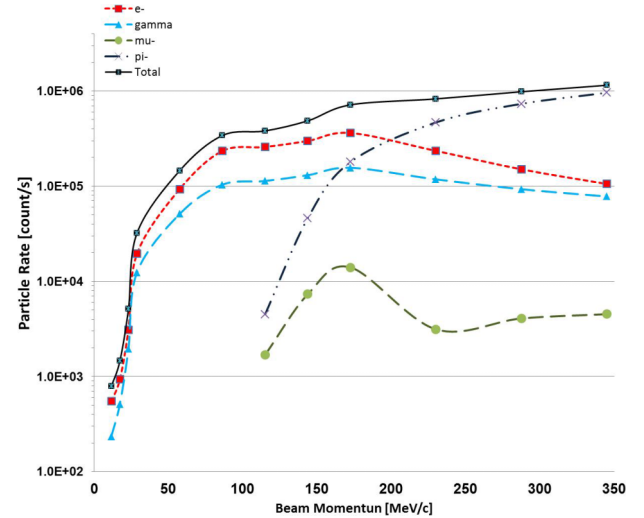
and gammas will be measured at the same time as primary electrons.

2. Beam composition by MCP detector: Analysis of counts distribution in the function of gain

The signals delivered by the MCP detector are current pulses that are converted to voltage pulses at the input impedance of oscilloscope 2. Due to the necessary trigger level settings ($\Delta V = -2.5$ mV) applied on the oscilloscope 2, pulses with lower amplitude cannot be measured by this method. The fraction of the events of lower amplitude, which are undetected, can be, however, deduced from the analysis of the counts distribution in the function of gain. The analysis of this distribution provides information on the detector operational characteristics (e.g., detector gain and MCP charge extraction).

For regular particles without penetrating power (e.g., keV ions), the pulses measured by the MCP detector form a peaked pulse height distribution. In contrast, for penetrating radiation, the shape of the counts distribution can be approximated by a negative exponential function (Fig. 12). A quasi-Gaussian pulse amplitude distribution, which sometimes broadens due to high rate of the investigated particles is often observed in the measurements of the particles with the energies up to a few tens of keV.[35,43,21] The particles measured here have energies larger than 10 MeV and can easily penetrate the MCP material and produce secondary electrons far from the front MCP surface. Hence, the initial secondary electron is not released at the entrance of a channel, but anywhere along the channel. By penetrating deeper in the channel, the electron will produce avalanche events with lower amplification. Because of this MCP signal generation mechanism, the amplification along the channel is an exponential function of the channel length that is available for amplification. As the result, an exponential shape of the counts distribution is obtained; the counts distribution is observed to decrease exponentially with increasing pulse amplitude. Also the MCP amplification together with the charge extraction is observed to be low.
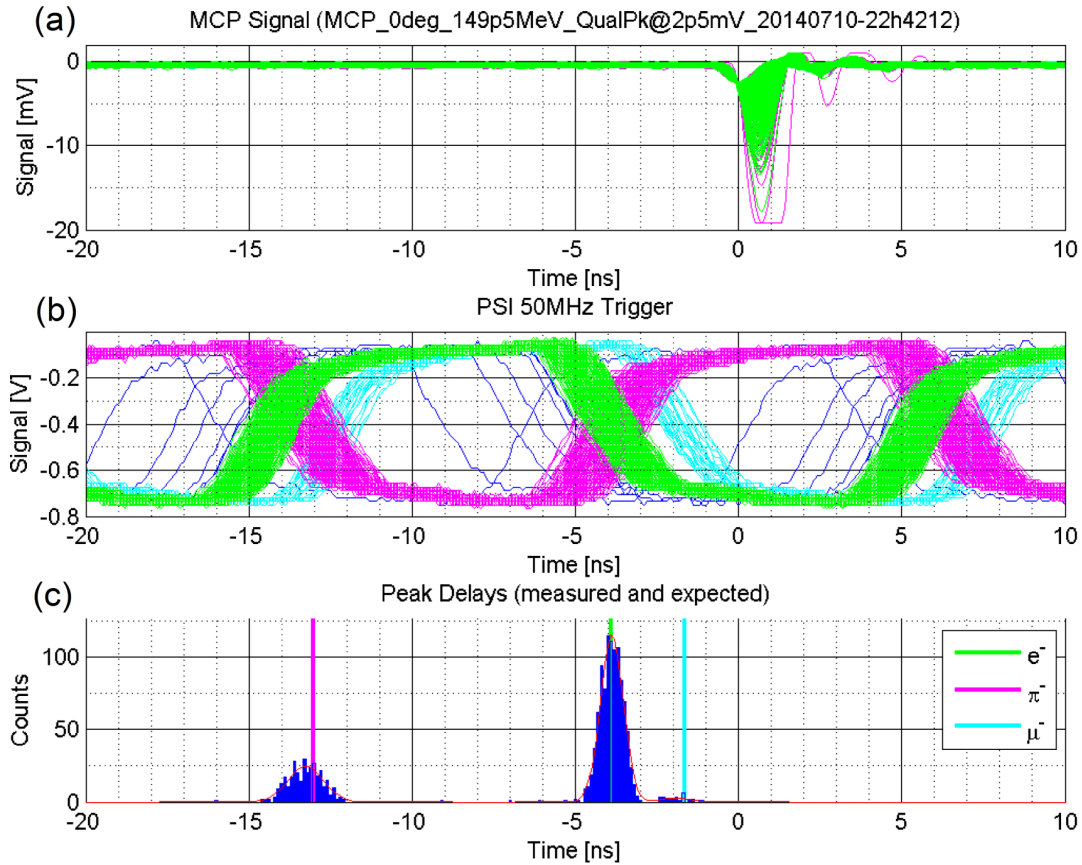
FIG. 11. The measurements of the beam composition. (a) The waveforms acquired by the measurement oscilloscope of the pulses which were produced by the MCP detector by the incident particles at the beam momentum of 149.5 MeV/c. (b) The 50 MHz cyclotron waveforms acquired simultaneously with the MCP measurements. Three main groups of phase-shifted waveforms are related to the time of the detection of the incident e⁻, μ⁻, and π⁻ particles, as indicated by the colour coding. (a) The histogram of the separated MCP counts according to their flight time. The assignment of the observed groups to the incident e⁻, μ⁻, and π⁻ particles is made by taking into account their calculated arrival times and is shown by the vertical lines shown in panel (c).

An exponential counts distribution shape was observed so far in particle detection by a single MCP,[44] but for MCP detector applied in chevron or z-stack configuration, typically, a peaked quasi-Gaussian PHD are observed.[45] Nevertheless, a negative exponential was reported also in the detection of gamma radiation, which easily penetrates the material to some depth before releasing first secondary electron.[46,47] Fig. 12 displays the counts distribution of electrons in the function of gain measured for the beam momentum 149.5 MeV/c.

To determine MCP gain and finally detection efficiency, single event statistics has been applied. This means, within one measurement, every single voltage peak has been analysed separately. By calculating the area of the peak, its charge has been determined. Since one peak originates from a single event, the gain is, in principle, directly this charge per peak divided by the unit charge e. To improve statistics, a histogram of this gain per peak has been made for all events in one measurement (see Fig. 12). This histogram shows an exponential distribution, which is expected for a high energy penetrating radiation, where the electron avalanche is started in an arbitrary depth of the MCP channel. Therefore, an exponential fit has been applied to the histogram to determine the mean gain thereof.

In addition, the exponential fit has been used to extrapolate the missing events below trigger level. The total

number of events within the measurement, e.g., acquisition time gives then the measured count rate, which can be divided by the known input particle rate to obtain the detection efficiency of the MCPs.
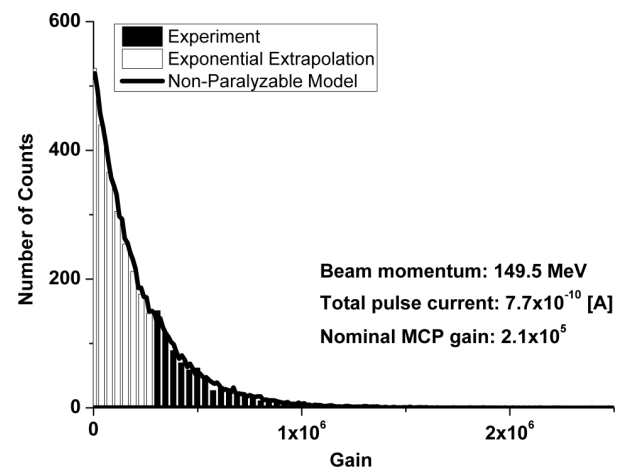

FIG. 12. Counts distribution in the function of gain measured for the electron beam momentum of 149.5 MeV/c (black histogram bars). An exponential distribution from the model is fit in gain values to the measurements to extrapolate the results below the trigger level at the low amplitude region (white histogram bars). The parameters determined from the PHD analysis are inserted in the figure. The count distribution predicted by applying non-paralyzable model is scaled to the measured histogram.
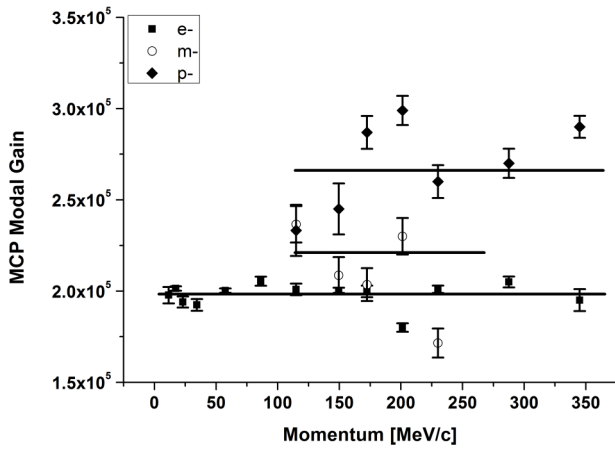
FIG. 13. MCP gains for the e⁻, μ⁻, and π⁻ particles determined from their counts distributions measured at various beam momenta. Horizontal bars give the average values for the measurements.
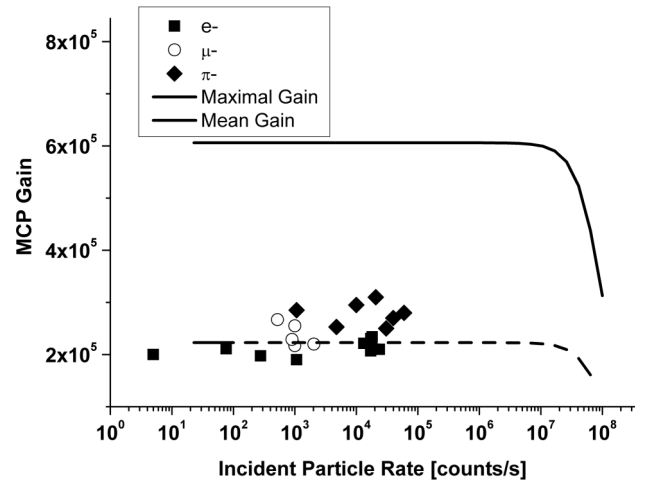

FIG. 14. Experimental results of the MCP nominal gain as function of the pulse rate are compared with the gains predicted from the non-paralyzable counter model. The model predicts that a possible saturation of the MCP detector is expected for the rates larger than 10^7 particles/s.

Fig. 13 displays the MCP nominal gains determined from the counts distribution of e⁻, μ⁻, and π⁻ particles and their secondaries, respectively. The nominal gain is a mean gain determined from the counts distribution. The gain values appear to be constant in the range of the investigated beam momenta for all particles. For the electrons, the values of the MCP gain are slightly smaller than for muons and pions. The reproducibility of the values was tested by repeating the measurements at least three times. The uncertainties of the determined gain values were found to be about 20%. Relatively low gain and low extracted charge values determined from the MCP measurements are consistent with the exponential shape of counts distribution and the mechanism of the pulse formation for penetrating radiation.

The incident particle rate increases with the beam momentum (Fig. 6). For the electron and pion beams, the particle rates of about 10^5 counts/s are observed in the beam momenta ranges 70–200 and 200–345 MeV/c, respectively. For the measurements of low energy particles (∼keV), these high rates can lead to saturation effects in MCP detectors and to decrease of the detector performance.[29,48] Above some critical particle rate, the charge depleted from the channel wall may not be fully replenished before the detection of following up event, which results in a reduction of MCP gain and counting efficiency. In the current investigation, the MCP nominal gain values are observed to be constant for particle rates up to 10^5 counts/s and no detector saturation effects were observed (see Fig. 13).

To explore the count-rate dependence on the nominal gain and determine a critical channel excitation rate of the MCPs used in the present study, a simple non-paralyzable-counter model was applied.[13,29] The model is based on an exponential recovery of the detector gain with time after the MCP has detected an event. Furthermore, a MCP chevron stack simulation for gain and PHD has been done to compare the results to the measurement. The simulation of the gain per MCP channel is based on the formula for secondary electron production in MCP channels.[13] Additionally, a non-paralyzable counter model has been used to statistically combine all MCP channels to an effective gain, taking into

account saturation effects by increased input flux rate or MCP dead-time at fixed number of channels. At the end, the propagation of mean fluxes through both MCP plates yields an overall gain. As input of the model, geometrical and physical parameters were taken from the MCP datasheet and the actual measurement setup. The counts distribution has been simulated using a two-step Monte Carlo method by first sampling gain values from an initial distribution and then sampling from a rate-reduced gain again due to the non-paralyzable model.[29] Initially, an exponential distribution has been chosen for our case. For comparison with the measurement data, the simulated normalised gain was multiplied with the overall mean gain, described above, and counts with the area-parameter of the exponential fit from the measurement. The predictions of the model are displayed in Fig. 14 together with the measured counts distribution. The modelling results indicate that a decrease of the detector gain can be expected for particle rates larger than 10^7 counts/s that are at least 10 times larger than those applied in the present investigations. The modelling results predict also the MCP gain dependence on electron rate under assumption that the MCP signal is produced by penetrating particles at some depth inside the MCP channel. The MCP modal gain dependence on electron rates under assumption that the counts distribution is close to a negative exponential is very similar to the experimental results (Fig. 14). The applied model predicts also counts distribution that is consistent with the experimental results (Fig. 12). High-energy particles penetrate deeper into the MCP channel and extract less current from the detector, which still can be refilled without observable saturation of the detector.

3. MCP count rates

Fig. 15 displays MCP count rates determined from the analysis of the measurements of e⁻, μ⁻, and π⁻ particles and background radiation for the various beam momenta applied in the current studies. Each data point is average of 3 to 5 measurements and the statistical errors due to fitting procedure
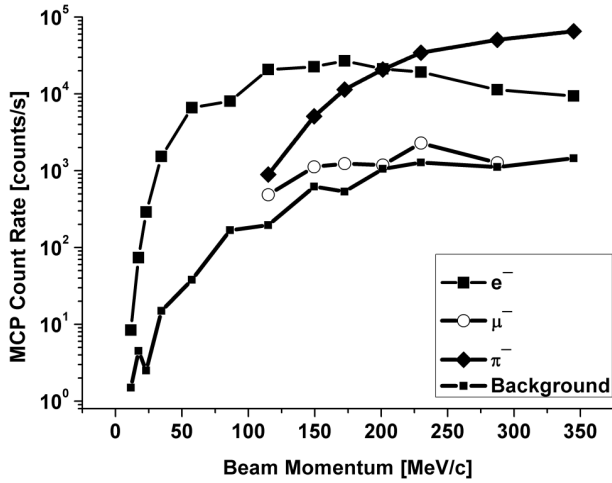
FIG. 15. Comparison of the MCP rates for the e$^-$, μ$^-$, and π$^-$ particles measured as a function of beam momentum. The background rates represent all counts that do not fit to any of three particle pulse height groups within 3σ (Fig. 7, panel C).

FIG. 16. MCP detection efficiency for the e$^-$, μ$^-$, and π$^-$ particles determined for various incident particle momenta. Horizontal lines give the average values for electrons (5.8% ± 0.5%) and pions (6.0% ± 1.3%), respectively.

are not expected to be larger than 5% for electrons and pions. For muons, small MCP count rates comparable to that of background radiation were measured and the measurements are less accurate. Background counts are observed to increase with an increase of the beam momentum.

C. MCP detection efficiency

MCP detection efficiencies for e$^-$, μ$^-$, and π$^-$ particles were defined in the Section II C above. To calculate the detection efficiencies, the primary particle rate is taken as predicted from the modelling studies and the contribution from the secondary particles is subtracted from the measured MCP counting rates. The MCP count rates of gamma ray and secondary electrons were determined taking into account the MCP detection efficiency of 2% and 16%, respectively.[18,19,27,47] The latter value was determined for electrons with the energies in the range of 50-100 keV, similar to that obtained in modelling (Fig. 8). From the GRAS/Geant4 model of the transmission of muons and pions, we derive only negligible corrections to the incident particle rate. Hence, the values determined from the analysis of primary beam incident rate and the MCP counting rates represent the final experimental values. For muons, the rate of secondary background electrons is comparable to that of primary muons which results in poor accuracy of the measurement (see Fig. 15). Background electrons affect also the values of the detection efficiency to pions at momentum 149 MeV/c and electrons at momentum 345.5 MeV (Fig. 16, data points in rectangular frame).

The averages of the detection efficiency values are 5.8% ± 0.5% for electrons in the beam momenta range 17.5–300 MeV/c and 6.0% ± 1.3% for pions in the beam momenta range 172–345 MeV/c. The stated uncertainties do not include the contribution from secondary electrons and gamma radiation. For secondary electrons, both the formation rate and the MCP detection efficiency vary readily with the secondary electron energy. Using the detection efficiency of
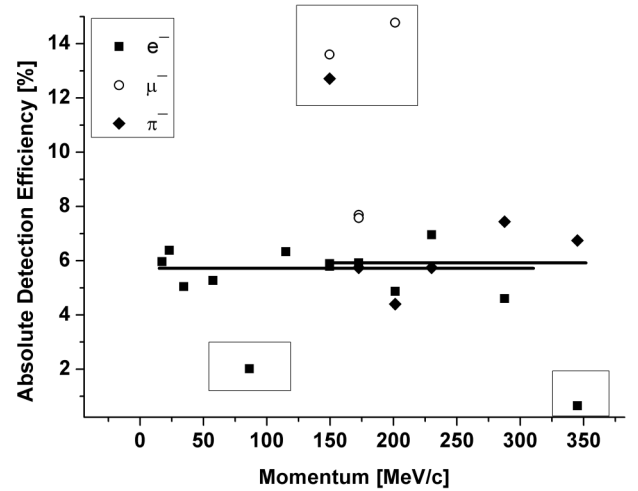
16% for the detection of secondary electrons, taking into account, a moderate decrease of their rate in the energy range from tens of MeV down to 20 keV (Fig. 8). For smaller electron energies, the detection efficiency is high but the rate contribution is limited with cutoff at 1.9 keV. In comparison with the measurement errors, the error due to uncertainty of the estimation of the correction due to secondary electron contribution is expected to smaller than the measurement error. For gamma radiation, the detection efficiency is expected to be relatively constant in the energy range with highest rate level (Fig. 9). Also in this case, the error of the correction applied in this study is expected to be smaller than the measurement error.

Due to a relatively low rate of incident muons and low MCP count rates comparable with the background radiation counts, the MCP detection efficiency to muons could not be determined accurately (see Fig. 16). A thinner window foils and an increase of measurement time for improvements of counting statistics would be necessary to reduce the measurement uncertainties.

IV. SUMMARY

- The detection efficiency of the MCP detector was investigated using high rate high-energy e$^-$, μ$^-$, or π$^-$ beams with momenta in the range 17.5–345 MeV/c. The measurements provided the quantitative characterisation of the beam composition and the absolute detection efficiency of these particles. The MCP signals were analysed by the PHD method, with a distribution that is described by a negative exponential function. Detector performance features, including charge extraction and modal gains, were determined. Low detector modal gains and extracted charges were found to be consistent with the mechanism of the MCP signal generation in the interior of MCP channel. The results from the modelling by paralyzable detector method confirmed the experimental results.

- Absolute detection efficiencies for e⁻ and π⁻ were determined to be $5.8\% \pm 0.5\%$ for electrons in the beam momenta range 17.5–300 MeV/c and $6.0\% \pm 1.3\%$ for pions in the beam momenta range 172–345 MeV/c. One of the important conclusions from this study is that at the investigated particle energies, even high rate of particles do not cause saturation of the detector. This will be of advantage when using this detector in Jovian environment.

- With the knowledge of the detection efficiency for penetrating electrons, both modelling and experimental investigation can be conducted to optimise radiation shielding against the radiation expected at the Jovian satellites.

- Current data can be useful for the development of highly sensitive MCP particle detector for experiments in high-energy physics.

ACKNOWLEDGMENTS

[1] O. Grasset, M. K. Dougherty, A. Coustenis, E. J. Bunce, C. Erd, D. Titov, M. Blanc, A. Coates, P. Drossart, L. N. Fletcher, H. Hussmann, R. Jaumann, N. Krupp, J. P. Lebreton, O. Prieto-Ballesteros, P. Tortora, F. Tosi, and T. Van Hoolst, Planet. Space Sci. **78**, 1 (2013).

[2] D. Abplanalp, P. Wurz, L. Huber, I. Leya, E. Kopp, U. Rohner, M. Wieser, L. Kalla, and S. Barabash, Adv. Space Res. **44**, 870 (2009).

[3] P. Wurz, D. Abplanalp, M. Tulej, and H. Lammer, Planet. Space Sci. **74**, 264 (2012).

[4] P. Wurz, D. Abplanalp, M. Tulej, M. Iakovleva, V. A. Fernandes, A. Chumikov, and G. G. Managadze, Sol. Syst. Res. **46**, 408 (2012).

[5] P. D. Fieseler, S. M. Ardalan, and A. R. Frederickson, IEEE Trans. Nucl. Sci. **49**, 2739 (2002).

[6] N. Divine and H. B. Garrett, J. Geophys. Res. **88**, 6889, doi:10.1029/JA088iA09p06889 (1983).

[7] D. J. Williams, R. W. Mcentire, S. Jaskulek, and B. Wilken, Space Sci. Rev. **60**, 385 (1992).

[8] K. P. Klaasen, M. J. S. Belton, H. H. Breneman, A. S. McEwen, M. E. Davies, R. J. Sullivan, C. R. Chapman, G. Neukum, and C. M. Heffernan, Opt. Eng. **36**, 3001 (1997).

[9] D. O. Kataria, J. Vac. Sci. Technol. B **24**, 1040 (2006).

[10] B. R. Sandel, A. L. Broadfoot, and D. E. Shemasky, Appl. Opt. **16**, 1533 (1977).

[11] O. H. W. Siegmund, K. Kromer, P. Wurz, R. Schletti, and H. Cottard, Proc. SPIE **4140**, 229 (2000).

[12] R. Rispoli, E. De Angelis, L. Colasanti, N. Vertolli, S. Orsini, J. A. Scheer, A. Mura, A. Milillo, P. Wurz, S. Selci, A. M. Di Lellis, R. Leoni, M. D'Alessandro, F. Mattioli, and S. Cibella, Opt. Eng. **52**, 051206 (2013).

[13] J. L. Wiza, Nucl. Instrum. Methods **162**, 587 (1979).

[14] T. Bouchama and M. Druetta, Nucl. Instrum. Methods Phys. Res., Sect. B **40–41**, 1252 (1989).

[15] B. L. Peko and T. M. Stephen, Nucl. Instrum. Methods Phys. Res., Sect. B **171**, 597 (2000).

[16] R. A. Schrack, Nucl. Instrum. Methods Phys. Res. **222**, 499 (1984).

[17] A. Baldin, G. Feofilov, Y. Gavrilov, A. Tsvinev, and F. Valiev, Nucl. Instrum. Methods Phys. Res., Sect. A **323**, 439 (1992).

[18] P. V. Schmidt, L. Willmann, R. Abela, J. Bagaturia, W. Bertl, B. Braun, H. Folger, K. Jungmann, D. Mzavia, G. Z. Putlitz, D. Renker, T. Sakhelashvili, and L. Zhang, Nucl. Instrum. Methods Phys. Res., Sect. A **376**, 139 (1996).

[19] G. W. Fraser, Nucl. Instrum. Methods Phys. Res. **206**, 251 (1983).

[20] E. H. Eberhardt, Appl. Opt. **18**, 1418 (1979).

[21] G. W. Fraser, M. T. Pain, and J. E. Lees, Nucl. Instrum. Methods Phys. Res., Sect. A **327**, 328 (1993).

[22] C. A. Kruschwitz, M. Wu, and G. A. Rochau, Rev. Sci. Instrum. **82**, 023102 (2011).

[23] A. J. Guest, Proc. SID **29**, 193 (1988).

[24] G. W. Fraser, Nucl. Instrum. Methods A **291**, 595 (1990).

[25] A. Westman, G. Brinkmalm, and D. F. Barofsky, Int. J. Mass Spectrom. Ion Processes **169-170**, 79 (1997).

[26] M. I. Babenkov, V. S. Zhdanov, and S. A. Starodubov, Nucl. Instrum. Methods Phys. Res., Sect. A **252**, 83 (1986).

[27] G. W. Fraser, Nucl. Instrum. Methods A **221**, 115 (1984).

[28] G. W. Fraser, *X-Ray Detection by Superconducting Tunnel Junctions* in *Proceeding of the International Workshop*, *Naples, Italy* (World Scientific, 1991) pp. 1–17.

[29] G. W. Fraser, M. T. Pain, J. E. Lees, and J. F. Pearson, Nucl. Instrum. Methods Phys. Res., Sect. A **306**, 247 (1991).

[30] T. M. Stephen and B. L. Peko, Rev. Sci. Instrum. **71**, 1355 (2000).

[31] M. Galanti, R. Gott, and J. F. Renaud, Rev. Sci. Instrum. **42**, 1818 (1971).

[32] G. Moldovan, J. Matheson, G. Derbyshire, and A. Kirkland, Nucl. Instrum. Methods Phys. Res., Sect. A **596**, 402 (2008).

[33] D. K. Waterhouse and J. F. Williams, Rev. Sci. Instrum. **68**, 3363 (1997).

[34] R. P. Tornow, Meas. Sci. Technol. **1**, 576 (1990).

[35] G. Klingelhoefer, H. Wiacker, and E. Kankeleit, Nucl. Instrum. Methods Phys. Res., Sect. A **247**, 379 (1986).

[36] W. Hajdas, L. Desorgher, K. Deiters, D. Reggiani, T. Rauber, M. Tulej, P. Wurz, M. Luethi, K. Wojczuk, and P. Kalaczynski, J. Appl. Math. Phys. **2**, 910 (2014).

[37] R. Schletti, P. Wurz, S. Scherer, and O. H. Siegmund, Rev. Sci. Instrum. **72**, 1634 (2001).

[38] P. Wurz and L. Gubler, Rev. Sci. Instrum. **67**, 1790 (1996).

[39] J. Allison, K. Amako, J. Apostolakis, H. Araujo *et al.*, IEEE Trans. Nucl. Sci. **53**, 270 (2006).

[40] G. Santin, V. Ivanchenko, H. Evans, P. Nieminen, and E. Daly, IEEE Trans. Nucl. Sci. **52**, 2294 (2005).

[41] E. M. Henley and A. Garcia, *Subatomic Physics* (World Scientific, Singapore, 2007).

[42] O. H. W. Siegmund, J. Vallerga, and J. Wargelin, IEEE Trans. Nucl. Sci. **35**, 524 (1988).

[43] J. G. Timothy, Rev. Sci. Instrum. **52**, 1131 (1981).

[44] E. J. Gamboa, C. M. Huntington, E. C. Harding, and R. P. Drake, Rev. Sci. Instrum. **81**, 10E310 (2010).

[45] G. W. Fraser, A. D. Pearson, G. C. Smith, M. Lewis, and M. A. Barstow, IEEE Trans. Nucl. Sci. **30**, 455 (1983).

[46] B. T. A. McKee, A. T. Stewart, and J. Vesel, Nucl. Instrum. Methods Phys. Res., Sect. A **234**, 191 (1985).

[47] Y. T. Tanaka, I. Yoshikawa, K. Yoshioka, T. Terasawa, Y. Saito, and T. Mukai, Rev. Sci. Instrum. **78**, 034501 (2007).

[48] A. S. Tremsin, J. F. Pearson, G. W. Fraser, W. B. Feller, and P. White, Nucl. Instrum. Methods Phys. Res., Sect. A **379**, 139 (1996).